



## **Final Draft of the original manuscript**

Ebner, S.; Schnitzer, R.; Suppan, C.; Stark, A.; Liu, H.; Hofer, C.:  
**Characterization of carbides in Q&P steels using a  
combination of high-resolution methods.**  
In: Materials Characterization. Vol. 163 (2020) 110242.

First published online by Elsevier: 02.03.2020

<https://dx.doi.org/10.1016/j.matchar.2020.110242>

## Characterization of carbides in Q&P steels using a combination of high-resolution methods

Sandra Ebner<sup>a</sup>, Ronald Schnitzer<sup>a</sup>, Clemens Suppan<sup>b</sup>, Andreas Stark<sup>c</sup>, Hongwei Liu<sup>d</sup>, Christina Hofer<sup>a\*</sup>

<sup>a</sup> Department of Materials Science, Montanuniversität Leoben, Franz-Josef-Strasse 18, 8700 Leoben, Austria.

<sup>b</sup> voestalpine Stahl GmbH, voestalpine-Strasse 3, 4020 Linz, Austria.

<sup>c</sup> Institute of Materials Research, Helmholtz-Zentrum Geesthacht, Max-Planck-Strasse 1, 21502 Geesthacht, Germany.

<sup>d</sup> Australian Centre for Microscopy and Microanalysis, The University of Sydney, Sydney, NSW 2006, Australia.

\* Corresponding author: christina.hofer@unileoben.ac.at

Declaration of interest: none

### **Highlights**

- In-situ observation of carbide formation during partitioning
- Application of HEXRD, APT and TEM for carbide identification
- Detection of cementite ( $\theta$ ), Hägg ( $\chi$ )-carbides and NbC
- Carbide precipitation due to martensite tempering and austenite decomposition

### **Abstract**

Current strategies for the 3<sup>rd</sup> generation of advanced high strength steels focus on the creation of a multiphase microstructure containing substantial amounts of retained austenite to enhance the mechanical properties. In the case of quenching and partitioning (Q&P) steels, the stabilization of austenite is achieved by carbon diffusion from the supersaturated martensite into the austenite, but carbon partitioning is often jeopardized by competing reactions such as carbide formation. In the present study, in-situ high-energy X-ray diffraction (HEXRD) was used to study the transformation kinetics during Q&P processing, and especially carbide formation at higher partitioning temperatures.

It was found that this carbide precipitation resulted mainly from martensite tempering and partially also from a decomposition of the austenite. The detection of minor diffraction peaks that appeared during the partitioning step was assigned to  $\theta$ - and  $\chi$ -carbide formation, which was supported by correlative atom probe tomography (APT) and transmission electron microscopy (TEM). Additionally, NbC was detected by APT, but the amount was obviously too low to be detected by HEXRD. The applied methods are finally compared with regard to their applicability for carbide identification in Q&P steels.

## **Keywords**

Advanced high strength steels (AHSS); quenching and partitioning (Q&P); high-energy X-ray diffraction (HEXRD); atom probe tomography (APT); transmission electron microscopy (TEM); carbide precipitation;

## **1. Introduction**

Increasing demands in the automotive industry encourage the development of new steel grades with improved combination of strength and formability. Among these, the quenching and partitioning (Q&P) processed steels have attracted growing interest and are considered as one of the most promising concepts for lightweight body-in-white constructions [1–3]. During the Q&P heat treatment, a certain amount of supersaturated martensite is attained after austenitization by partially quenching to a temperature between the martensite start temperature ( $M_s$ ) and the martensite finish temperature ( $M_f$ ). Subsequently, the remaining austenite is stabilized via carbon enrichment from the supersaturated martensite during the so-called partitioning step. As a result, the high amount of tempered martensite enables high strength, while ductility is provided by the substantial amount of meta-stable austenite and the related transformation induced plasticity (TRIP) effect [4–6].

A key aspect of the Q&P concept is the stabilization of austenite by carbon diffusion. Unfortunately, the carbon content available for partitioning is often reduced due to carbon being trapped in the martensite by carbon clustering, carbon segregation, or carbide formation [7,8]. Although silicon alloying is used to avoid carbide formation [2,9,10], it was found to rather delay than completely prevent  $\theta$ -carbide formation. Moreover, the effect on the precipitation of transition carbides is not yet clear and might not be affected or even accelerated by silicon. Regarding Q&P processing,  $\theta$ -carbide, which appears preferentially at higher partitioning temperatures and prolonged holding [11–13],  $\epsilon$ - [14] and  $\eta$ -carbides [15] have been observed. Unfortunately, the investigation of carbides in Q&P steels is a challenging task. The use of laboratory X-ray diffraction (XRD) often fails to detect carbides at all due to the small volume fractions and consequently low intensities. Moreover, X-ray diffraction patterns of transition carbides are quite similar, and thus difficult to distinguish. The same problem arises in the case of transmission electron microscopy (TEM) due to the similar and complex electron diffraction patterns. Nevertheless, TEM is among the most commonly used methods for carbide identification. By this means, HajyAkbari et al. [14] detected the

precipitation of  $\epsilon$ -carbides in a 0.3C-1.6Si-3.5Mn (wt%) steel. These carbides were found to occur during the first quench and re-dissolve during partitioning at 400 °C. Transition carbides ( $\epsilon$  or  $\eta$ ) were also identified using TEM by Thomas et al. [8]. Furthermore, TEM was combined with Mössbauer effect spectroscopy (MES) by Pierce et al. [15]. This enabled both the identification and quantification of carbides in a 0.38C-1.48Si-1.54Mn (wt%) steel. They detected  $\eta$ -carbides after quenching to 225 °C and holding for 10 s. The amount increased from 1.4 to 2.4 at% during subsequent partitioning at 400 °C for 300 s. For a chemical analysis of the carbides at atomic scale, atom probe tomography (APT) can be used. Based on the local chemistry, carbides observed in a 0.59C-2.0Si-2.9Mn-0.038Al (wt%) steel after partitioning at 400 °C for 300 s were assigned as  $\theta$ -carbide by Toji et al. [13]. However, carbide identification based only on APT often remains uncertain, since the carbon content does not always match the stoichiometric composition of  $\theta$ -carbide (~25 at%),  $\eta$ -carbide (~29 at%) or  $\epsilon$ -carbide (~33 at%). Moreover, carbon quantification by APT might be affected by the loss of carbon due to a higher number of multiple hit events [16,17], or by the analysis condition, e.g. measurement temperature [18–20], which can result in an over- or underestimation of the carbon concentration.

An issue of the aforementioned methods is their limitation to the final heat-treated condition. Hence, the precipitation kinetics are not directly accessible, although this is of high interest to optimize partitioning parameters. Recently, Allain et al. [21] conducted in-situ high-energy X-ray diffraction (HEXRD) experiments to investigate carbide precipitation during Q&P processing of a 0.3C-2.5Mn-1.5Si (wt%) steel. The high signal to noise ratio allowed the detection of small diffraction peaks in addition to the main austenitic and martensitic peaks. These peaks appeared during reheating to the partitioning temperature of 400 °C and remained unchanged during partitioning. Due to similar diffraction patterns of the transition carbides, a clear identification by HEXRD turned out to be difficult, but  $\eta$ -carbides seemed most likely. The presence of  $\theta$ -carbide was ruled out, which was supported by correlative TEM observations.

In the present work, different high-resolution techniques, including in-situ HEXRD, TEM and APT, were combined for the first time to provide an advanced characterization of carbides formed during Q&P heat treatments. The advantages of in-situ HEXRD experiments were exploited for the real-time characterization of a Q&P steel partitioned at two different temperatures (360 and 420 °C). The qualitative and quantitative analysis of the recorded

diffraction patterns provided time-resolved information about the process of austenite decomposition and carbon partitioning into the austenite, as it was previously reported in literature [22–26]. The appearance of additional diffraction peaks indicated carbide formation during partitioning at 420 °C. The crystallographic information obtained from both HEXRD patterns and additional TEM investigations was used for carbide identification. Furthermore, APT was used to identify the occurring carbides by their chemical composition. In order to determine whether these carbides formed in martensite or austenite, a clear identification of martensitic and austenitic regions was necessary. The carbon content obtained from the APT measurements can serve as a basis for this distinction due to the generally higher carbon content in the austenite. To support the identification of austenitic regions in the atom probe tips, transmission Kikuchi diffraction (TKD) prior to the APT measurements was also applied. This method was already used successfully to identify and study retained austenite in TRIP-assisted steels [27]. Based on the obtained results, the applied methods are compared and their strengths and application limits for the investigation of carbide formation in Q&P steels are discussed.

## **2. Experimental procedure**

### **2.1 Investigated steel and heat treatments**

The chemical composition of the investigated steel is 0.2C/0.5-1.0Si/2.2-2.7Mn/<0.03Nb (wt%) or 0.9C/1.0-2.0Si/2.2-2.7Mn/<0.02Nb (at%), respectively. The martensite start temperature ( $M_s$ ) is 338 °C as determined by dilatometry. The material was provided in its cold-rolled condition in the form of sheets with a thickness of 1.1 mm. Samples of 10 x 4 mm<sup>2</sup> were cut and heat treated in a dilatometer DIL 805A/D from TA Instruments, using Al<sub>2</sub>O<sub>3</sub> rods and a type S thermocouple for temperature control. The heat treatments comprised austenitization at 850 °C, followed by a holding step at 750 °C for 10 s and subsequent quenching with 50 °C/s to a quenching temperature  $T_q$  of 230 °C. After 3 s at  $T_q$ , samples were reheated with 30 °C/s to the partitioning temperature  $T_p$ . Partitioning was conducted for 300 s either at 360 °C (HT360) or 420 °C (HT420). An overview of the conducted heat treatments can be seen in Figure 1.

The heat treated samples were grinded and polished by conventional metallographic methods followed by 3% Nital etching for a microstructural characterization in a scanning electron microscope (SEM) ZEISS EVO 50.

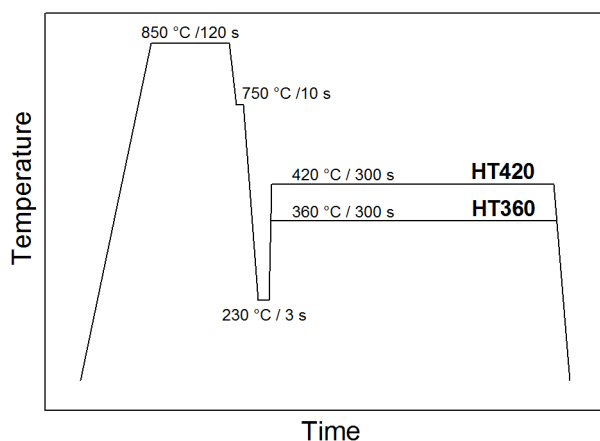


Figure 1: Schematic representation of the conducted heat treatments HT360 and HT420.

## 2.2 In-situ HEXRD

HEXRD experiments were executed at the P07 beamline of HZG at PETRA III, DESY, Germany [28]. During the entire heat treatments, diffraction patterns were recorded with a fast area detector (Perkin Elmer XRD 1621) using monochromatic synchrotron X-ray radiation with a photon energy of 100 keV ( $\lambda = 0.124 \text{ \AA}$ ). Additionally, a  $\text{LaB}_6$  standard sample was measured as reference. The obtained 2D data was azimuthally integrated using the Data Analysis Workbench (DAWN) [29,30]. A Rietveld refinement procedure implemented in the commercial software TOPAS from Bruker AXS applying the fundamental parameters approach was used to determine phase fractions and lattice parameters. The refinement included zero displacement, background, scale factors, unit cell parameters, temperature factors and texture parameters. To account for the instrumental contribution to the line profile shapes, the parameters of the instrumental function were determined by a fit of the  $\text{LaB}_6$  reference sample. The obtained values were fixed and used for the refinement procedure of the actual measurements. A double-Voigt approach was used for considering size and strain broadening effects [31].

## 2.3 Transmission electron microscopy

For TEM investigations, samples of HT420 were mechanically thinned to a thickness of 90  $\mu\text{m}$ . Subsequently, discs with a diameter of 3 mm were electropolished using 6 vol% perchloric acid in 94 vol% acetic acid at 15 °C with a flow rate of 31 and an applied voltage of 16 V. Final preparation comprised ion polishing using a GATAN precision ion polishing system (PIPS) with a first polishing step at 1 keV for 10 min followed by a second step at 0.5 keV for 5 min. The

TEM investigations were performed on a JEM-2200FS from JEOL operated at 200 kV at the University of Sydney, Australia. Indexing of the obtained diffraction patterns was supported by SP2 software [32].

#### 2.4 Atom probe tomography

Steel strips were subjected to the heat treatments (HT360, HT420) as described in 2.1 on an annealing simulator MULTIPAS. From these strips, atom probe tips were prepared by the standard double-layer and micropolishing method described in [33]. Prior to the APT measurements, the atom probe tips were examined via TKD in a dual-beam SEM/FIB Versa 3D from FEI equipped with a Hikary XP EBSD system from EDAX. TKD scans were carried out according to [34] at a working distance of 10 mm, an acceleration voltage of 20 kV, 4x4 binning and a step size of 3 nm. The TKD scans were analyzed using the TSL OIM Analysis 7 software applying a grain dilatation clean-up. This enabled a clear distinction of martensitic and austenitic regions. APT measurements were conducted in a local electrode atom probe (Cameca LEAP 3000X HR) either in voltage mode (pulse rate of 200 kHz, pulse fraction of 0.2, sample temperature of 60 K) or in laser mode (laser energy of 0.3 nJ, pulse rate of 250 kHz, sample temperature of 40 K) with a target evaporation rate of 0.5%. Data evaluation was performed with the Imago Visualization and Analysis Software (IVAS) version 3.6. Regarding carbon, peaks corresponding to  $C^+$ ,  $C^{2+}$ ,  $C_2^+$ ,  $C_3^+$ ,  $C_3^{2+}$  and  $C_4^{2+}$  were detected. The peak at 24 Da could be either due to  $C_2^+$ ,  $C_4^{2+}$  or a mixture of both. The peak at 25 Da could correspond to  $C_2^+$ ,  $C_4^{2+}$  or  $Cr^{2+}$ . Apart from these peaks, no further severe peak overlapping occurred, and thus no peak decomposition procedure was applied. Based on a comparison of the peak heights at 25 and 26 Da, both peaks were indexed as  $Cr^{2+}$ . The peak at 24 Da was assigned to  $C_2^+$ , which might lead to a slight underestimation of the detected carbon concentration.

### **3. Results and discussion**

#### 3.1 Evolution of phase fraction and austenite lattice parameter

Figure 2a shows exemplary integrated 1D diffraction patterns recorded at different heat treatment stages of HT360. Peaks corresponding to austenitic or ferritic (i.e. ferrite/bainite/martensite) phase can be clearly identified. The material was fully austenitized at 850 °C. During the subsequent cooling and holding at 750 °C, peaks of ferritic phase appeared, but the signal was too low for a quantitative analysis. These ferritic peaks became

more pronounced on further cooling and indicated the formation of ferrite and bainite prior to the formation of martensite. Fitting of the diffraction data just before the onset of martensite transformation revealed an amount of ferrite/bainite below 3%. At  $M_s$  (338 °C) austenite rapidly transformed, resulting in a martensite fraction of around 86% at the end of the quenching step (230 °C). During partitioning (360 °C) until the end of the heat treatment the major austenitic and ferritic diffraction peaks only changed slightly. For the fitting procedure, austenite was modelled by using a face-centered cubic cell (fcc, Fm-3m). The ferritic peaks were fitted by a body-centered cubic cell (bcc, Im-3m) above  $M_s$ , and then by a body-centered tetragonal cell (bct, I4/mmm) to meet the predominantly martensitic fraction. The resulting microstructure after HT360 and HT420 can be seen in Figure 2b and c, respectively. The microstructure predominantly consists of tempered martensite (strongly etched areas) with fine austenite films and austenite islands (raised features). Occasionally, small platelets appear in the tempered martensite, that likely represent carbides.

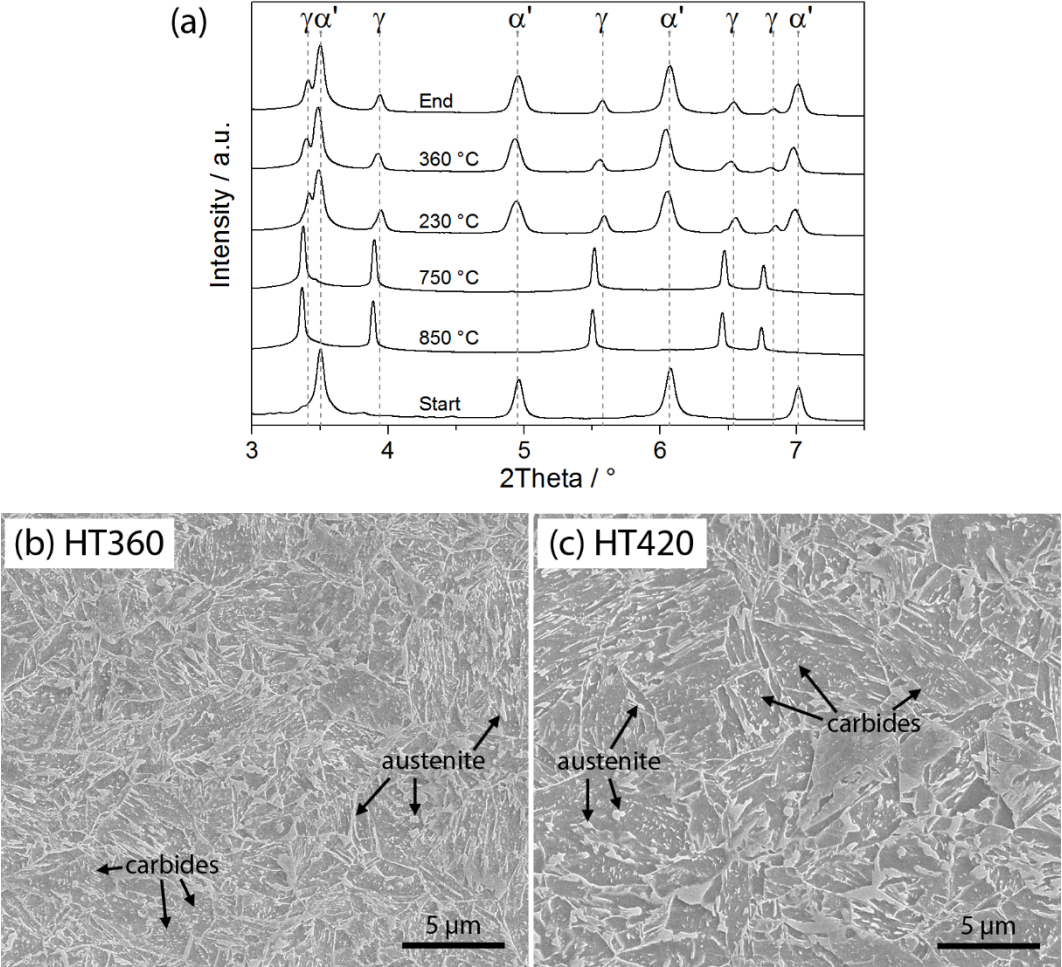


Figure 2: (a) 1D diffraction patterns recorded at different heat treatment stages during HT360; SEM images of (b) HT360 and (c) HT420.

The temporal evolution of austenite fraction and austenite lattice parameter after the end of the quenching step is shown in Figure 3. The individual stages of reheating, partitioning and final cooling are separated by vertical lines. As can be seen in the upper graph of Figure 3, the austenite fraction  $f_\gamma$  decreases from 14% to 7% during partitioning. Note that  $f_\gamma$  does not change during the final cooling, which suggests that no fresh martensite formed and austenite was sufficiently stabilized to room temperature. Simultaneously to the austenite decomposition, which is most pronounced at the very beginning of partitioning, the austenite lattice parameter  $a_\gamma$  rapidly increases (center graph in Figure 3). While the curve constantly increases for HT360, a fast initial dilatation can be seen for HT420 that reaches its maximum after 40 s. Afterwards, the curve decreases again.

There are several factors influencing  $a_\gamma$ , i.e. temperature, carbon content and stress states. To exclude the thermal contribution, a correction of the lattice parameter was executed considering an exponential coefficient of thermal expansion (CTE) in accordance to the procedure described by Allain et al. [25]. The coefficients necessary for the calculation of CTE were obtained by the fit of dilatometer curves in the range of 400 to 800 °C. It has to be mentioned that in this way the influence of internal stresses is not considered for the correction of  $a_\gamma$ , despite the work of Allain et al. [25] showed that the austenite is subjected to complex stresses along the entire Q&P heat treatment. The resulting difference curve  $a_{diff}$  obtained after subtracting the calculated from the measured lattice parameter values can be seen in the lowest graph of Figure 3. The measured dilatation of  $a_{diff}$  by the end of partitioning allowed an estimation of the carbon enrichment in the austenite. During the final quench, it is assumed that the carbon content remains unchanged, and the observed increase of  $a_{diff}$  is attributed to internal stresses arising upon cooling [25]. Using the relation given in [23] ( $da_\gamma = 0.033 dC_\gamma$ ), the measured dilatation during partitioning for HT360 ( $1.99 \times 10^{-2} \text{ \AA}$ ) can be referred to a carbon increase of 0.60 wt%. For HT420, the maximum increase ( $1.76 \times 10^{-2} \text{ \AA}$ ) after 40 s corresponds to a carbon content of 0.53 wt%, while the increase by the end of partitioning ( $1.51 \times 10^{-2} \text{ \AA}$ ) yields a lower value of 0.46 wt%. The final amount of carbon in the austenite can be estimated to be around 0.80 wt% (3.64 at%) for HT360 and 0.66 wt% (3.00 at%) for HT420.

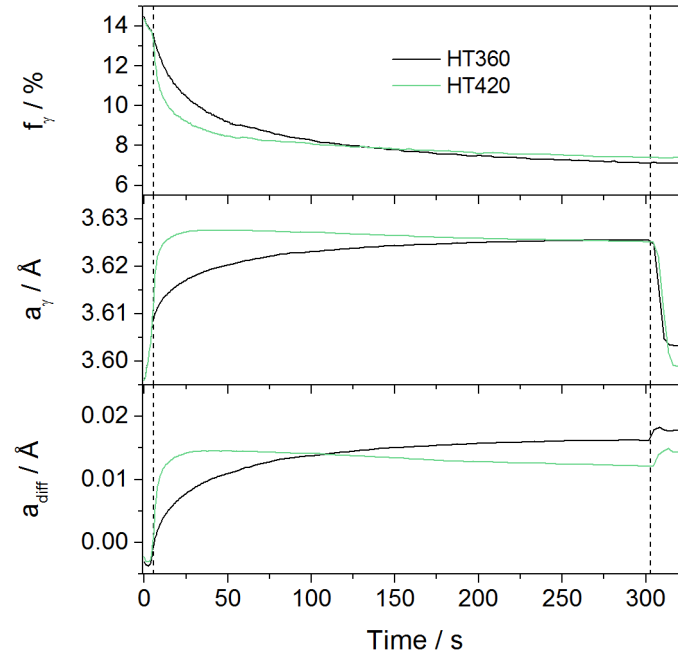


Figure 3: Temporal evolution of austenite phase fraction ( $f_\gamma$ ), measured austenite lattice parameter ( $a_\gamma$ ), and difference between calculated and measured austenite lattice parameter ( $a_{diff}$ ). Note that  $t = 0$  s indicates the end of the quenching step. Reheating, partitioning and final cooling are divided by vertical lines.

Since carbon enrichment causes an expansion of  $a_\gamma$ , the contraction of  $a_\gamma$  seen for HT420 may indicate carbon depletion due to austenite decomposition accompanied by carbide formation. These findings are supported by the work of Bigg et al. [35], who also observed such a decrease using in-situ neutron diffraction during partitioning of a 0.64C-4.57Mn-1.30Si (wt%) steel, albeit at different partitioning conditions ( $M_s$  below room temperature, slow heating from room temperature to a  $T_p$  of 500 °C and a total measuring time of 3 h). Furthermore, decomposition of austenite at high  $T_p$  was also reported in [11–13].

For both HT360 and HT420,  $f_\gamma$  decreases during partitioning. Since there is no indication of austenite decomposition by carbide formation for HT360 (i.e. no decrease of  $a_\gamma$ ), it can be concluded that in both cases the decline of austenite fraction is mainly caused by bainite formation, which is known to also compete with carbon partitioning [14,36,37]. Assuming that the entire decrease of  $f_\gamma$  is caused by the formation of bainite, about 7% bainite is formed regardless of the chosen  $T_p$ . Even if carbide formation contributes to an austenite decomposition in the case of HT420, the decrease of  $f_\gamma$  observed after 40 s is below 2%, and thus small compared to the decrease caused by bainite formation that occurs particularly at the beginning of partitioning.

Besides the HEXRD patterns, the dilatometer signal was also recorded during the in-situ experiments and the temporal evolution of the relative length change during the partitioning step is shown in Figure 4 (solid lines). Since the use of  $\text{Al}_2\text{O}_3$  push rods, as it was the case for the HEXRD experiments, affects the accuracy of the dilatometer measurement to a greater extent than  $\text{SiO}_2$  push rods, the heat treatments were also conducted on a dilatometer 805A using  $\text{SiO}_2$  rods. The results are shown in Figure 4 as dashed lines. Using  $\text{Al}_2\text{O}_3$  rods, both curves continuously increase during partitioning. With the use of  $\text{SiO}_2$  rods, a contraction is observed for HT420 starting after 40 s of partitioning, while the curve continuously increases and finally levels off for HT360. The dilatometer curve represents the sum of the expansion caused by bainite formation – and to a smaller extent also by carbon enrichment in the austenite – and the contraction caused by carbon depletion of the martensite, either through carbon partitioning into the austenite or carbide formation [38]. Thus, from the dilatometer curves seen in Figure 4 it can be concluded that partitioning and bainite formation are the main processes at 360 °C, while martensite tempering effects dominate at 420 °C.

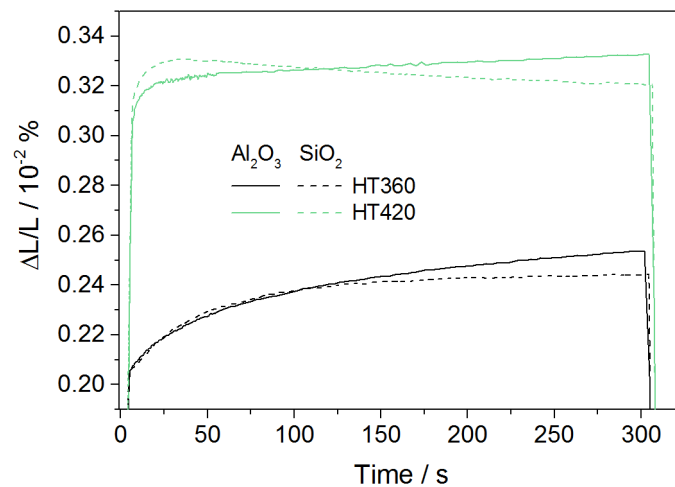


Figure 4: Measured relative length change during partitioning at 360 °C and 420 °C using  $\text{Al}_2\text{O}_3$  (solid lines) and  $\text{SiO}_2$  (dashed lines) rods.

### 3.2 Carbide identification by HEXRD

In order to detect even small amounts of carbides that form during partitioning with HEXRD, the diffraction patterns were carefully examined and some are with exemplary results shown in Figure 5 for HT360 (upper graph) and for HT420 (lower graph). Indeed, minor diffraction peaks in addition to the main austenitic and martensitic peaks can be seen, although some peaks might be better defined as humps than clear peaks. During the austenitization step, few

peaks appear that are marked by red arrows. Compared to the diffraction pattern recorded at the end of austenitization (red line), there are no additional peaks at the beginning of partitioning (blue line). By the end of partitioning (green line) and at the end of the heat treatment (black line), further peaks can be seen for HT420 (lower graph in Figure 5), which are marked by black arrows. For HT360, there is only a sluggish hump visible at  $3^\circ$  (upper graph in Figure 5, black arrow).

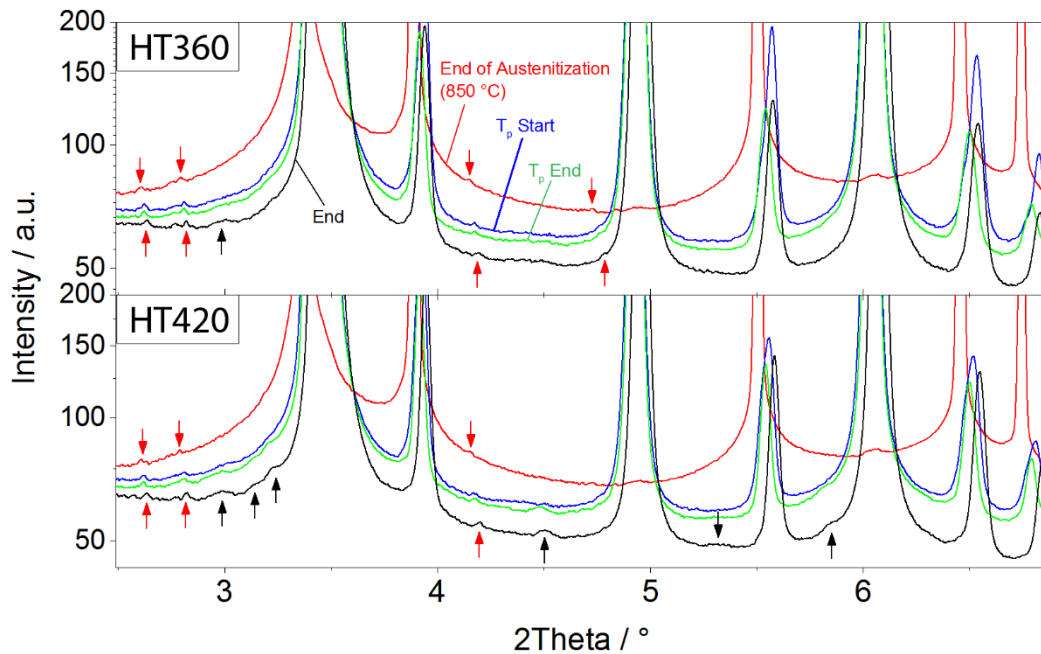


Figure 5: Enlarged section of diffraction patterns (log scale) at different heat treatment stages for HT360 and HT420.

For the identification of the additional peaks, patterns obtained from the Powder Diffraction File (PDF) database of the International Centre of Diffraction Data (ICDD) were compared to the present patterns. With regard to iron carbides previously found in Q&P steels,  $\theta$ -carbide [39],  $\eta$ -carbide [40] and  $\epsilon$ -carbide [41] were considered. Additionally, also the  $\chi$ -carbide [42] and NbC [43] were taken into account, whereby the detection of NbC by HEXRD was assumed to be unlikely, since the low Nb-addition allows the formation of a maximum of 0.034 wt% NbC.

The diffraction pattern obtained at the end of HT420 together with the respective hkl peak locations of the considered carbides are shown in Figure 6a-e. It can be seen that the most prominent peaks of the iron carbides (Figure 6a-d) are around  $3.5^\circ$ , and thus highly overlap with major peaks of the diffraction pattern. Moreover, pattern positions of the iron carbides are very close, which further impedes a simple identification. Regarding the peaks that appear

during partitioning (black arrows in Figure 5), a good match was found for  $\theta$ -carbide (Figure 6a). The positions of  $\chi$ -carbide (Figure 6b) fit with the peaks at  $3.22^\circ$  and  $4.5^\circ$ . The peaks at  $3^\circ$  and  $3.22^\circ$  also coincide with those of  $\epsilon$ -carbide (Figure 6c). The worst match can be seen for  $\eta$ -carbide in Figure 6d. As expected, NbC can be ruled out, since the most prominent peak at  $2.75^\circ$  is missing (Figure 6e). No match with the considered carbides was found for the peaks that formed during austenitization (red arrows in Figure 5). Considering a possible oxidation of the sample's surface during austenitization, patterns of iron oxides were additionally taken into account, and indeed a good match is found for  $\text{Fe}_2\text{O}_3$  [44] as can be seen in Figure 6f.

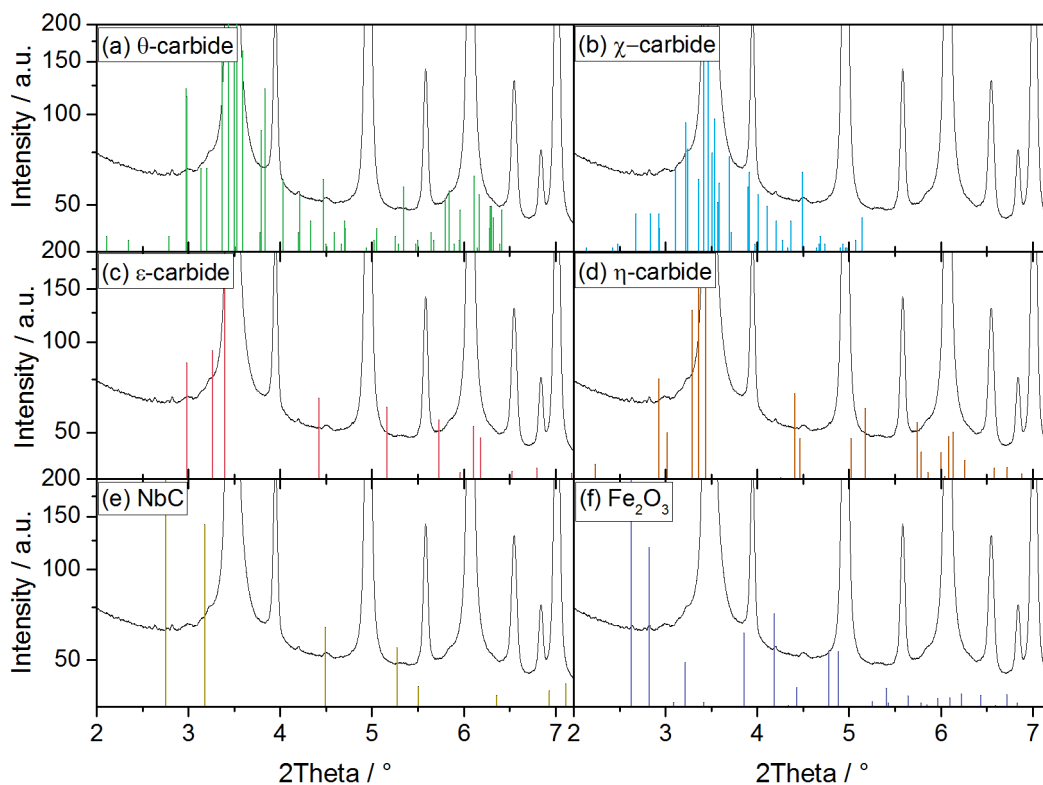


Figure 6: Diffraction pattern (log scale) of HT420 sample at the end of the heat treatment showing the hkl peak locations for (a)  $\theta$ -carbide, (b)  $\chi$ -carbide, (c)  $\epsilon$ -carbide, (d)  $\eta$ -carbide, (e) NbC and (f)  $\text{Fe}_2\text{O}_3$ .

A comparison of the diffraction patterns recorded during partitioning revealed a first clear distinctness of carbide peaks from the background after about 120 s, which is delayed compared to the contraction observed by dilatometry after 40 s (Figure 4). This is supposed to be reasonable, since a minimum phase volume is necessary to obtain diffraction patterns at all, and moreover carbon segregation and clustering prior to carbide formation does not generate diffraction patterns, but may already lead to a contraction visible in the dilatometer.

### 3.3 Carbide identification by TEM

The comparison of the diffraction peaks with different carbide diffraction patterns revealed that  $\theta$ -carbide is most likely present in the microstructure, but the occurrence of transition carbides cannot be excluded. Moreover, the decrease of  $a_\gamma$  detected by HEXRD (Figure 3) indicates carbide formation next to or in the austenite, but a considerable amount certainly precipitated in the martensitic matrix due to martensite tempering. To further study the carbides formed during partitioning, TEM investigations were carried out on HT420. Figure 7a shows a bright field (BF) image of martensite containing plate-like precipitates with a length of about 250 nm and a thickness of 15 nm. These precipitates can be identified as  $\theta$ -carbide based on the selected area electron diffraction (SAED) pattern shown in Figure 7b. Since the SAED pattern was not taken from preferred orientation, conclusions regarding the orientation relationship (OR) between martensite and  $\theta$ -carbide are difficult to draw, but it is expected to coincide with the OR typically found for martensite and  $\theta$ -carbide, i.e. Bagaryatskii [45] or Isaichev [46] OR.

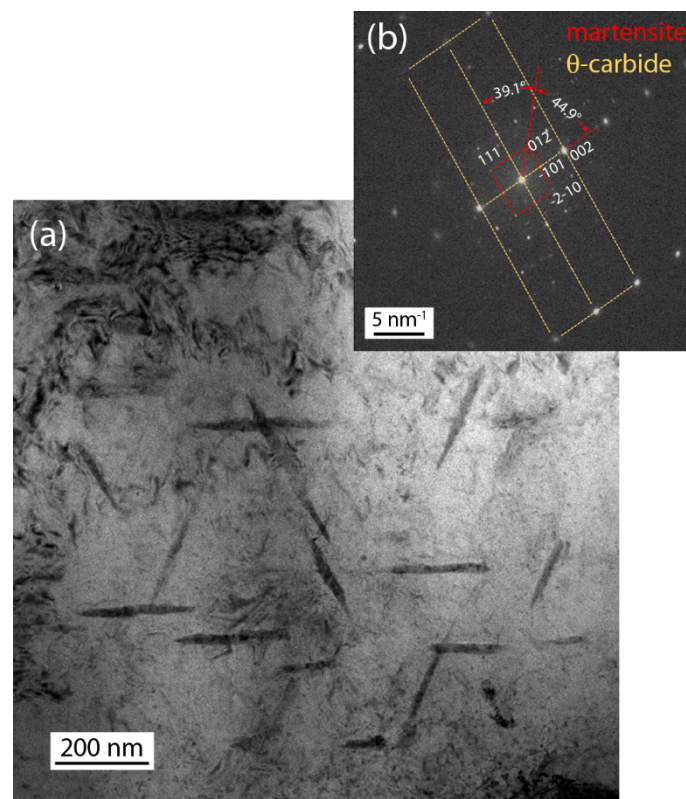


Figure 7: (a) BF image of martensite containing  $\theta$ -carbides with plate-like morphology (HT420); (b) SAED pattern of  $\theta$ -carbide with  $[1\bar{2}1]_\theta$  zone axis and martensite with  $[5\bar{3}3]_M$  zone axis.

Figure 8a shows a HRTEM image, where a single spherical carbide with a diameter of around 10 nm is embedded in austenite. Analysis of the crystal structure of the observed carbide was done utilizing fast Fourier transformation (FFT). The FFT for austenite with diffraction zone axis close to  $[\bar{1}10]_A$  is depicted in Figure 8b, that of the carbide can be indexed as monoclinic  $\chi$ -carbide with zone axis nearby  $[1\bar{3}5]_\chi$  (Figure 8c). Indexing of this phase has taken into account the conversion of index number between plane and plane normal that is often different for low symmetric crystals, such as hexagonal or orthorhombic structures.

In order to derive a statistically relevant OR between two phases, it is necessary to collect a sufficient number of composited electron diffraction patterns or FFT images that contain both phases. Due to the low number of  $\chi$ -carbides in the present case, this is difficult to achieve. One possible OR between austenite and  $\chi$ -carbide can be extracted from the FFT image in Figure 8d that was generated from an area covering both austenite and carbide:

$$\begin{aligned} &[\bar{1}10]_A \parallel [1\bar{3}5]_\chi \\ &(220)_A \parallel (310)_\chi \\ &(111)_A \parallel (121)_\chi. \end{aligned} \quad (1)$$

The above expression of the observed OR can be reorganized to low index plane and direction by applying composited stereographic projection (SP). Figure 8e shows the directional SP of austenite with pole center at  $[010]_A$  overlapped with directional SP of  $\chi$ -carbide centered at  $[132]_\chi$ . Due to the cubic crystal of austenite, the index in the SP can be referred to plane normal or direction. However, for the monoclinic  $\chi$ -carbide, the plane normal (hkl) is generally not the same as [uvw] even though they have the same numbers. For easy reading, plane normal and direction indices are underlined. The zone axis  $[\bar{1}10]_A \parallel [1\bar{3}5]_\chi$  indicated in Figure 8d can be found in the SP and is marked as 'zone axis of FFT'. The observed parallel planes  $(220)_A \parallel (310)_\chi$  and  $(111)_A \parallel (121)_\chi$  can be also found in the SP. Thus, equation (1) for the observed OR can be simplified to

$$\begin{aligned} &(010)_A \parallel (11\bar{1})_\chi \\ &[100]_A \parallel [112]_\chi \\ &[001]_A \parallel [\bar{1}32]_\chi. \end{aligned} \quad (2)$$

Considering the cubic structure of austenite, equation (2) can be further written as:

$$\begin{aligned} &(001)_A \parallel (11\bar{1})_\chi \\ &[100]_A \parallel [112]_\chi \end{aligned} \quad (3)$$

$$[010]_A \parallel [\bar{1}32]_\chi$$

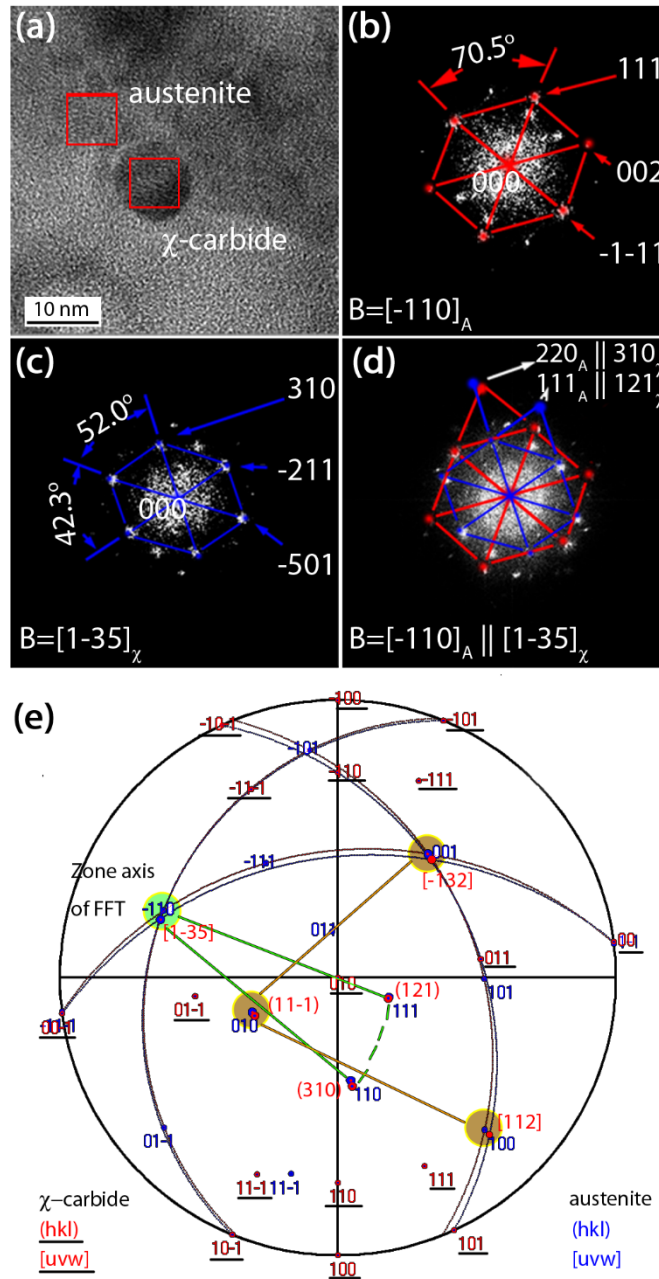


Figure 8: (a) HRTEM image of HT420 showing spherical  $\chi$ -carbide embedded in austenite; (b) FFT image from austenite with  $[-110]_A$  zone axis; (c) FFT image of  $\chi$ -carbide with zone axis along  $[1\bar{3}5]_\chi$ ; (d) composed FFT corresponding to both austenite and  $\chi$ -carbide providing information of possible OR; (e) composed directional stereographic projection (SP) of austenite  $[010]_A$  and  $\chi$ -carbide  $[132]_\chi$  derived from FFT shown in (d).

### 3.4 Carbide identification by APT

APT measurements were conducted on the HT420 condition. This not only enabled a chemical analysis of the occurring carbides, but provided also information about the carbide formation sites. Figure 9a shows the carbon atom map and isoconcentration surfaces with different carbon thresholds of 0.95 at% (nominal carbon content), 5 at% and 15 at%. Apart from a carbon-rich feature, the carbon concentration in the matrix is low (<1 at%), which supports the identification as a martensitic region. The calculated proximity histogram based on the 15 at% isoconcentration surface is shown in Figure 9b. The carbon concentration increases to about 25 at%. The manganese content slightly increases, while a clear reduction of silicon is visible. The other alloying elements are distributed uniformly and are thus not presented here.

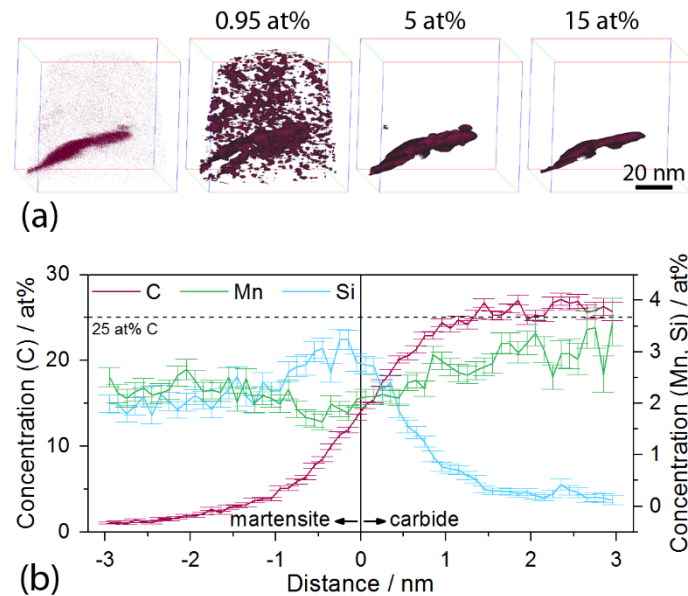


Figure 9: APT measurement (voltage mode) of HT420: (a) carbon atom map and carbon isoconcentration surfaces (0.95, 5 and 15 at%); (b) proximity histogram of the iron carbide defined by 15 at% isoconcentration surface.

Another APT measurement of HT420 is depicted in Figure 10a, showing the carbon distribution map and the isoconcentration surfaces of 5 and 15 at% carbon. The overall carbon concentration of the entire measurement volume is substantially higher than the nominal concentration, with a highly enriched area indicated by the 15 at% carbon isoconcentration surface. The respective proximity histogram of the region indicated by an arrow is shown in Figure 10b. The carbon concentration increases from 5 at% to 25 at%, while manganese does not change. Again, silicon partitioning is obvious.

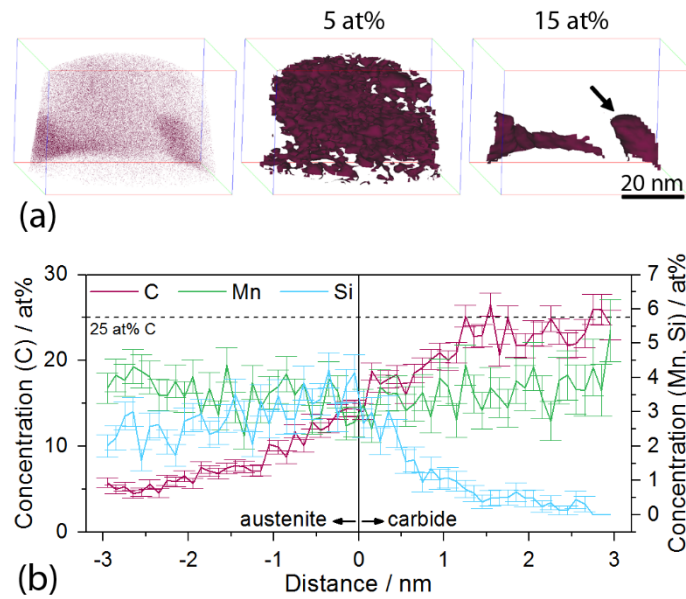


Figure 10: APT measurement (voltage mode) of HT420: (a) carbon atom map and carbon isoconcentration surfaces (5 and 15 at%); (b) proximity histogram of the iron carbide defined by 15 at% isoconcentration surface (marked by an arrow).

The high carbon concentration measured in the atom probe tip shown in Figure 10a indicates an austenitic region, but high carbon concentrations might also be measured for martensite that formed from the carbon-enriched austenite during the final quench. The presence of fresh martensite is assumed unlikely, since no further decrease of  $f_{\gamma}$  upon cooling was detected by HEXRD (Figure 3). However, unambiguous identification of austenite based on APT is not possible without crystallographic information. For this reason, a TKD scan was conducted prior to the APT measurement, which was carried out in laser mode in order to prevent early sample fracture. As can be seen in Figure 11a, austenite was observed within the obtained TKD pattern, which confirmed that the top of the atom probe tip shown in Figure 11b corresponds to an austenitic region. A non-homogeneous carbon distribution can be seen, with a carbon-rich region at the top of the tip (Figure 11c) and a carbon-depleted region at the bottom, including some carbon- and niobium-enriched areas (Figure 11d).

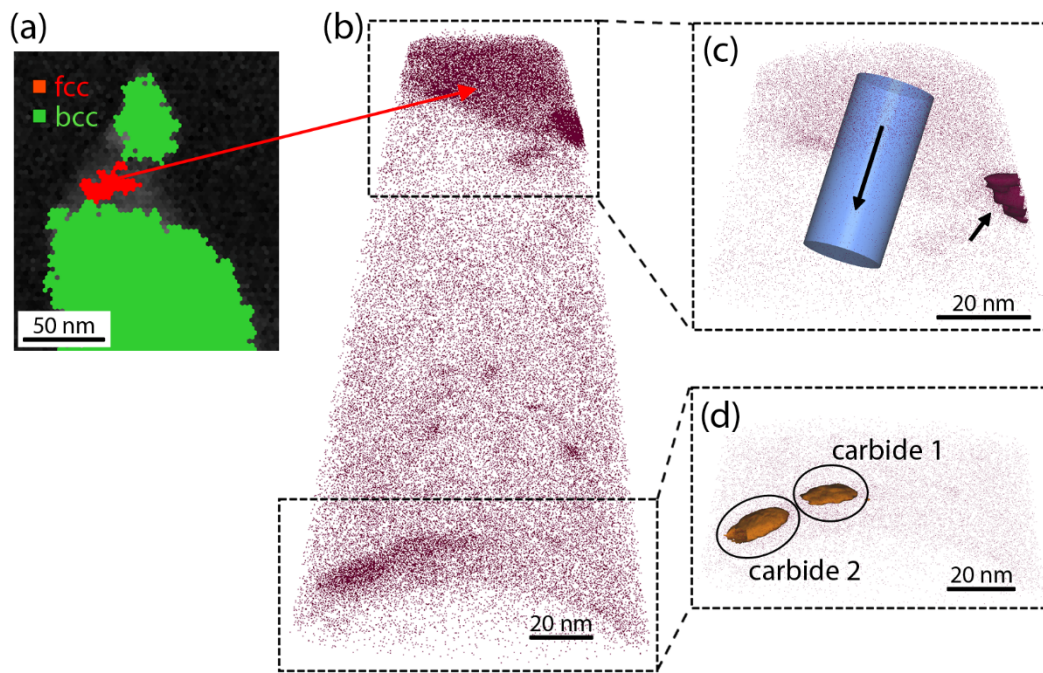


Figure 11: APT measurement (laser mode) of HT420: (a) TKD scan of the atom probe tip prior to the APT measurement; (b) carbon atom map; (c) enlarged section of the upper part of the atom probe tip shown in (b) indicating 15 at% carbon isoconcentration surface; (d) enlarged section of the lower part of the atom probe tip shown in (b) indicating 2 at% niobium isoconcentration surface.

A 1D concentration profile across the austenite/martensite interface was calculated along the cylinder marked in Figure 11c and the result is shown in Figure 12a. While the silicon content stays unchanged across the interface, a pile-up of manganese can be seen on the austenite side of the interface. This indicates partitioning of small amounts of manganese, which was also reported in other studies [5,7,47]. A clear increase of the carbon concentration from 0.25 at% in the martensite to 3 at% in the austenite was determined. The 15 at% carbon isoconcentration surface seen in Figure 11c indicates an area with even higher carbon concentration at the edge of the tip. Figure 12b shows the proximity histogram of this surface. The amount of manganese increases, and also the carbon concentration increases to nearly 20 at%. A decrease of silicon was also detected.

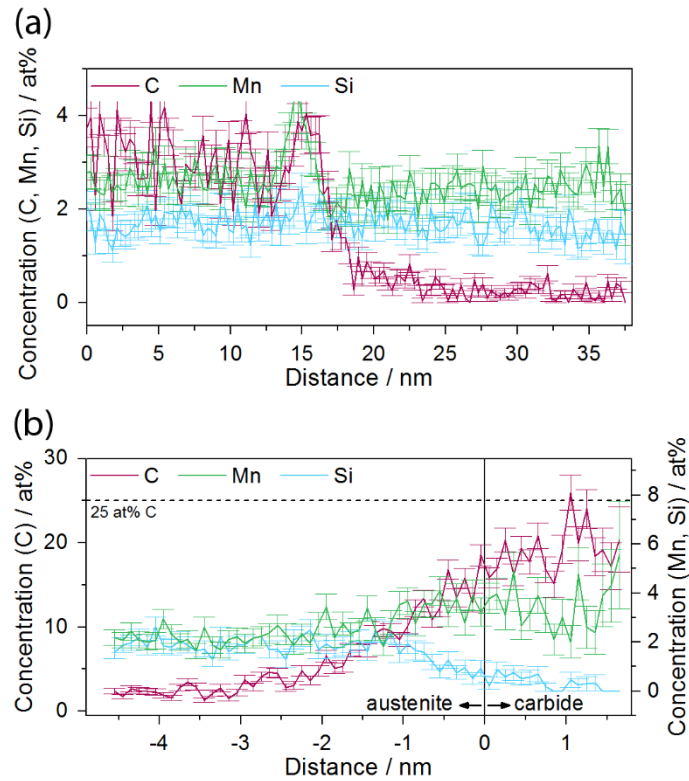


Figure 12: (a) 1D concentration profile along the austenite/martensite interface as marked by the cylinder in Figure 9c; (b) proximity histogram of the iron carbide marked by an arrow in Figure 9c.

Indication of iron carbides were found in all presented atom probe tips. In the case of the measurements shown in Figure 9 and 10, the carbon concentration reaches 25 at%, which is the stoichiometric carbon composition of  $\theta$ -carbide. For the atom probe tip shown in Figure 11, the carbon concentration is slightly below 25 at%, but it is only a very small edge of the carbide that has been detected. The decrease of silicon that was observed for all measurements and also the slight manganese enrichment seen in Figure 9b and 12b are a strong indication that the detected carbides are indeed  $\theta$ -carbide. Several authors report a repulsion of silicon at the early stages of  $\theta$ -carbide formation followed by a gradual enrichment of manganese with prolonged tempering [9,13,48,49]. However, definitive carbide identification remains a subject of uncertainty due to the issues of carbon quantification encountered with APT. The carbon concentration may be underestimated due to carbon atoms that can get 'lost' during APT measurements because of more frequent multiple hit events and the dead time of the detector [16]. Furthermore, the quantitative analysis of APT measurements also depends on the analysis condition. For example, lower sample temperatures are preferential to minimize the difference in the evaporation fields of

the different elements, but parameter studies in voltage mode showed that a decreasing measurement temperature resulted in an overestimation of the nominal carbon concentration of  $\theta$ -carbide [18,19]. This was attributed to a loss in the detection of iron ions [19]. Regarding laser-pulsed APT, it was found that the detected carbon concentration in  $\theta$ -carbide increased with lower laser pulse energies, which was also attributed to a loss of iron ions due to a detector pile-up [20]. In addition, no peak decomposition was applied in the present work and the assignment of the peak at 24 Da to  $C_2^+$  might lead to an underestimation of the carbon content. Nevertheless, the observed manganese enrichment and silicon depletion plead for an assignment of the detected iron carbides as  $\theta$ -carbide.

Proximity histograms of the observed niobium-enriched features shown in Figure 11d were calculated and the results are shown in Figure 13. The other alloying elements do not change and are thus not shown. The question arises whether these NbC have formed during partitioning or before. Regarding cold-rolled sheets, Speer et al. [50] stated that NbC precipitation should be fairly completed at latest after annealing, and is thus unlikely to occur during partitioning. There are several studies concerning niobium alloying in Q&P steels, where NbC was clearly identified by TEM [51–55] and precipitation during the partitioning step was suggested. Though, clear evidence for NbC formation during partitioning can be only found in [52]. In this work, a 0.485C-1.195Mn-1.185Si-0.98Ni-0.21Nb (wt%) steel was subjected to a quenching-partitioning-tempering process with a combined partitioning-tempering step at 400 °C for 10 or 1800 s. Four different types of carbides were detected, among them fine NbC that nucleated in lath martensite during partitioning. However, the niobium content of the steel investigated in the present work is much lower, and further studies are considered necessary to provide clarity whether NbC precipitates during partitioning or before in the case of low Nb-containing Q&P steels.

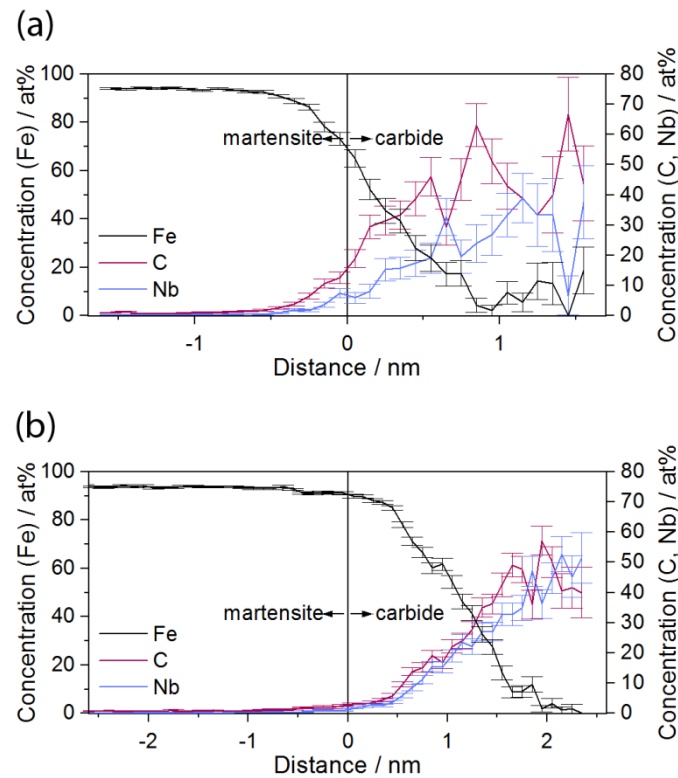


Figure 13: Proximity histograms of (a) carbide 1 and (b) carbide 2 as marked in Figure 9d.

### 3.5 Comparison of the applied investigation methods

First indication of carbide formation can be derived from the SEM images shown in Figure 2b and c, where small platelets are occasionally visible in the tempered martensite for both HT360 and HT420. Further evidence is obtained from dilatometry, which presents a fast and easy accessible method to gain an overview of the phase transformations taking place during partitioning. The contraction seen during partitioning at 420 °C (Figure 4) results from stronger martensite tempering, and consequently a higher carbide fraction was expected. Carbide precipitation could be followed by in-situ HEXRD (Figure 5) and the marginal appearance of additional diffraction peaks during partitioning at 360 °C (Figure 5) confirmed that the carbide volume fraction of HT360 is obviously lower than that of HT420, but the carbide volume fraction of both heat treatments was too small for a quantitative analysis. Moreover, a clear carbide identification turned out to be difficult, because the peak positions of the different iron carbides are in close vicinity, as can be seen in Figure 6. Another drawback regarding the qualitative analysis of HEXRD patterns is that it is not possible to distinguish between the carbides formed in martensite, which certainly contribute the most to the detected signal, and carbides formed as a result of austenite decomposition. The additional information obtained

from the in-situ HEXRD experiments, i.e. the temporal evolution of  $a_\gamma$  seen in Figure 3, clearly shows that austenite is affected by the carbide formation, resulting in a decrease of the austenite carbon content from 0.73 wt% after 40 s to 0.66 wt%.

TEM investigations enabled a simultaneous identification of precipitates and the surrounding matrix. Among the applied techniques, it is also the only method that revealed information about the carbide morphology. Regarding APT measurements, it was also possible to distinguish between carbides, austenite and martensite based on the different carbon concentration, which allows a distinction of the carbide formation in austenitic or martensitic regions. The additional combination with TKD and the obtained crystallographic information facilitates a clear phase identification and supports site-specific measurements of austenitic regions and adjacent iron carbides. However, it must be emphasized that the TKD patterns are primarily derived from the bottom 10 – 20 nm of the atom probe tip facing the EBSD camera [56]. In order to examine the whole tip, additional scans after sample rotation are necessary. Furthermore, the detection of carbides by TKD in the investigated steel is unlikely due to the resolution limits of this technique (5-10 nm [57]). In addition, not the entire tip volume is obtained in the atom probe due to its limited field of view [58]. Nevertheless, both APT and TEM are indispensable to support carbide identification, and moreover they also enable the characterization of smallest amounts of precipitates (in this case NbC by APT), that were not detectable by HEXRD.

While  $\theta$ -carbide formation resulting from martensite tempering and/or austenite decomposition is in accordance with previous studies [11-13],  $\chi$ -carbides have not been detected in Q&P steels so far. Martensite tempering involving a  $(\epsilon, \eta) \rightarrow \chi \rightarrow \theta$ -carbide sequence have been reported [59-62], and furthermore tempering of a 1.22 wt% C steel revealed that austenite could decompose not only into  $\theta$ -carbide (and ferrite), but also into  $\chi$ -carbide (and ferrite) [63]. Moreover, further studies are necessary to investigate the impact of the associated carbon depletion of the austenite on its stability, albeit the austenite decomposition resulting from carbide formation was found to be negligible compared to the austenite decomposition by bainite formation. The austenite fraction of both HT360 and HT420 is 7% (see Figure 3), but the estimated carbon content in the austenite is around 0.14 wt% lower for HT420. Together with the stronger tempering of the surrounding martensite at 420 °C, which was reported to negatively affect the mechanical stability of

austenite [64], this may result in a reduced austenite stabilization that consequently affects formability. Furthermore, there is a lack of information about the influence of carbide formation in Q&P steels on the mechanical properties. Minor effects are expected by small amounts of transition carbides, while excessive  $\theta$ -carbide growth might deteriorate ductility. In this case, a shortening of the partitioning time, especially at higher temperatures, would be necessary.

#### **4. Summary**

In the present work, two different Q&P cycles, including quenching to 230 °C and subsequent partitioning at 360 °C or 420 °C for 300 s, were studied by means of different high-resolution characterization methods. In-situ HEXRD was carried out to study the processes taking place during the heat treatments. During partitioning, the austenite fraction decreased from about 14% to 7%, which was attributed to bainite formation. A rapid increase of the austenite lattice parameter at the very beginning of partitioning revealed clear carbon enrichment of the austenite. After 40 s at 420 °C, the austenite lattice parameter decreased again, which resulted in a lower austenite carbon content of 0.66 wt% compared to 0.80 wt% after partitioning at 360 °C. This decrease indicated carbide formation taking place as a result of austenite decomposition.

Based on the obtained HEXRD patterns, the onset of carbide formation could be followed by the occurrence of additional diffraction peaks, which were found to appear during partitioning at 420 °C after about 120 s. These peaks could be most likely assigned to  $\theta$ - and  $\chi$ -carbide, but it was not possible to draw definite conclusions about the nature of carbides or their formation sites without additional information. Hence, additional TEM and APT investigations were conducted that confirmed the existence of  $\theta$ -carbide formed as a result of martensite tempering. Furthermore,  $\chi$ -carbide embedded in austenite was detected by TEM. The assumption of austenite decomposition by carbide precipitation was also supported by APT measurements, where austenite, which was unambiguously identified by a prior TKD scan of the atom probe tip, and adjacent carbides were detected. These carbides could be identified as cementite based on the local chemistry. Finally, NbC were also detected by APT, but it remains unclear, whether NbC precipitated during partitioning or not, since the amount was apparently too low to be visible in the diffraction pattern.

## **Acknowledgments**

Funding of the Austrian BMVIT (846933) in the framework of the program “Production of the future” and the “BMVIT Professorship for Industry” is gratefully acknowledged. We acknowledge DESY (Hamburg, Germany), a member of the Helmholtz Association HGF, for the provision of the experimental facilities. Parts of this research were carried out at PETRA III and we would like to thank Dr. Nobert Schell for assistance at the P07 high-energy materials science (HEMS) beamline. In addition, the authors thank Dr. Andreas Landefeld for the assistance during the HEXRD experiments. Special thanks to Dr. Michael Tkadletz, Dr. Christian Saringer and Dominik Nöger for their support regarding data processing, and Dr. Mehdi Eizadjou and Jacob Byrnes for their assistance in TEM sample preparation.

## **Data availability**

The raw/processed data required to reproduce these findings cannot be shared at this time as the data also forms part of an ongoing study.

## **References**

- [1] J.G. Speer, D.K. Matlock, B.C. De Cooman, J.G. Schroth, Carbon partitioning into austenite after martensite transformation, *Acta Mater.* 51 (2003) 2611–2622. doi:10.1016/S1359-6454(03)00059-4.
- [2] J.G. Speer, A.M. Streicher, D.K. Matlock, F. Rizzo, G. Krauss, Quenching and partitioning: A fundamentally new process to create high strength TRIP sheet microstructures, *Mater. Sci. Technol. 2003 Meet.* (2003) 505–522.
- [3] G.A. Thomas, J.F. Hansman, Development, design, and industrial launch of next-generation steel, in: *Int. Symp. New Dev. Adv. High Strength Sheet Steels*, Keystone, USA, 2017: pp. 11–18.
- [4] E. De Moor, S. Lacroix, A.J. Clarke, J. Penning, J.G. Speer, Effect of retained austenite stabilized via quench and partitioning on the strain hardening of martensitic steels, *Metall. Mater. Trans. A.* 39 (2008) 2586–2595. doi:10.1007/s11661-008-9609-z.
- [5] E.J. Seo, L. Cho, Y. Estrin, B.C. De Cooman, Microstructure-mechanical properties relationships for quenching and partitioning (Q&P) processed steel, *Acta Mater.* 113 (2016) 124–139. doi:10.1016/j.actamat.2016.04.048.
- [6] S. Ebner, C. Suppan, R. Schnitzer, C. Hofer, Microstructure and mechanical properties of a low C steel subjected to bainitic or quenching and partitioning heat treatments, *Mater. Sci. Eng. A.* 735 (2018) 1–9. doi:10.1016/j.msea.2018.08.026.
- [7] Y. Toji, H. Matsuda, M. Herbig, P.P. Choi, D. Raabe, Atomic-scale analysis of carbon partitioning between martensite and austenite by atom probe tomography and correlative transmission electron microscopy, *Acta Mater.* 65 (2014) 215–228. doi:10.1016/j.actamat.2013.10.064.
- [8] G.A. Thomas, F. Danoix, J.G. Speer, S.W. Thompson, F. Cuvilly, Carbon atom re-distribution during quenching and partitioning, *ISIJ Int.* 54 (2014) 2900–2906. doi:10.2355/isijinternational.54.2900.
- [9] G. Miyamoto, J.C. Oh, K. Hono, T. Furuhashi, T. Maki, Effect of partitioning of Mn and Si on the growth kinetics of cementite in tempered Fe-0.6 mass% C martensite, *Acta Mater.* 55 (2007) 5027–5038. doi:10.1016/j.actamat.2007.05.023.

- [10] E. Kozeschnik, H.K.D.H. Bhadeshia, Influence of silicon on cementite precipitation in steels, *Mater. Sci. Technol.* 24 (2008) 343–347. doi:10.1179/174328408X275973.
- [11] D. De Knijf, E.P. Da Silva, C. Föjer, R. Petrov, Study of heat treatment parameters and kinetics of quenching and partitioning cycles, *Mater. Sci. Technol.* 31 (2015) 817–828. doi:10.1179/1743284714Y.0000000710.
- [12] D.T. Pierce, D.R. Coughlin, D.L. Williamson, J. Kähkönen, A.J. Clarke, K.D. Clarke, J.G. Speer, E. De Moor, Quantitative investigation into the influence of temperature on carbide and austenite evolution during partitioning of a quenched and partitioned steel, *Scr. Mater.* 121 (2016) 5–9. doi:10.1016/j.scriptamat.2016.04.027.
- [13] Y. Toji, G. Miyamoto, D. Raabe, Carbon partitioning during quenching and partitioning heat treatment accompanied by carbide precipitation, *Acta Mater.* 86 (2015) 137–147. doi:10.1016/j.actamat.2014.11.049.
- [14] F. HajyAkbari, J. Sietsma, G. Miyamoto, T. Furuhashi, M.J. Santofimia, Interaction of carbon partitioning, carbide precipitation and bainite formation during the Q&P process in a low C steel, *Acta Mater.* 104 (2016) 72–83. doi:10.1016/j.actamat.2015.11.032.
- [15] D.T. Pierce, D.R. Coughlin, D.L. Williamson, K.D. Clarke, A.J. Clarke, J.G. Speer, E. De Moor, Characterization of transition carbides in quench and partitioned steel microstructures by Mössbauer spectroscopy and complementary techniques, *Acta Mater.* 90 (2014) 417–430. doi:10.1016/j.actamat.2015.01.024.
- [16] M. Thuvander, J. Weidow, J. Angseryd, L.K.L. Falk, F. Liu, M. Sonestedt, K. Stiller, H.-O. Andrén, Quantitative atom probe analysis of carbides, *Ultramicroscopy.* 111 (2011) 604–608.
- [17] R.K.W. Marceau, P. Choi, D. Raabe, Understanding the detection of carbon in austenitic high-Mn steel using atom probe tomography, *Ultramicroscopy.* 132 (2013) 239–247.
- [18] J. Takahashi, K. Kawakami, Y. Kobayashi, Quantitative analysis of carbon content in cementite in steel by atom probe tomography, *Ultramicroscopy.* 111 (2011) 1233–1238. doi:10.1016/j.ultramic.2011.03.024.
- [19] G. Miyamoto, K. Shinbo, T. Furuhashi, Quantitative measurement of carbon content in Fe-C binary alloys by atom probe tomography, *Scr. Mater.* 67 (2012) 999–1002. doi:10.1016/j.scriptamat.2012.09.007.
- [20] H.S. Kitaguchi, S. Lozano-Perez, M.P. Moody, Quantitative analysis of carbon in cementite using pulsed laser atom probe, *Ultramicroscopy.* 147 (2014) 51–60. doi:10.1016/j.ultramic.2014.06.004.
- [21] S.Y.P. Allain, S. Aoued, A. Quintin-Poulon, M. Gouné, F. Danoix, J.-C. Hell, M. Bouzat, M. Soler, G. Geandier, In-situ investigation of the iron carbide precipitation process in a Fe-C-Mn-Si Q&P steel, *Materials (Basel).* 11 (2018) 1087. doi:10.3390/ma11071087.
- [22] T. Rieger, K. Herrmann, D. Carmele, S. Meyer, T. Lippmann, A. Stark, W. Bleck, U. Klemradt, 'Quenching and Partitioning' - an in-situ approach to characterize the process kinetics and the final microstructure of TRIP-assisted steel, *Adv. Mater. Res.* 409 (2011) 713–718. doi:10.4028/www.scientific.net/AMR.409.713.
- [23] S.Y.P. Allain, G. Geandier, J.-C. Hell, M. Soler, F. Danoix, M. Gouné, In-situ investigation of quenching and partitioning by high energy X-ray diffraction experiments, *Scr. Mater.* 131 (2017) 15–18. doi:10.1016/j.scriptamat.2016.12.026.
- [24] S.Y.P. Allain, G. Geandier, J.-C. Hell, M. Soler, F. Danoix, M. Gouné, Effects of Q&P processing conditions on austenite carbon enrichment studied by in situ high-energy X-ray diffraction experiments, *Metals (Basel).* 7 (2017) 232. doi:10.3390/met7070232.
- [25] S.Y.P. Allain, S. Gaudez, G. Geandier, J. Hell, M. Gouné, F. Danoix, M. Soler, S. Aoued, A. Poulon-Quintin, Internal stresses and carbon enrichment in austenite of quenching and partitioning steels from high energy X-ray diffraction experiments, *Mater. Sci. Eng. A.* 710 (2018) 245–250. doi:10.1016/j.msea.2017.10.105.
- [26] S. Ebner, C. Suppan, A. Stark, R. Schnitzer, C. Hofer, Austenite decomposition and carbon partitioning during quenching and partitioning heat treatments studied via in-situ X-ray diffraction, *Mater. Des.* 178 (2019) 107862. doi:10.1016/j.matdes.2019.107862.

- [27] C. Hofer, F. Winkelhofer, H. Clemens, S. Primig, Morphology change of retained austenite during austempering of carbide-free bainitic steel, *Mater. Sci. Eng. A*. 664 (2016) 236–246. doi:10.1016/j.msea.2016.04.005.
- [28] N. Schell, A. King, F. Beckmann, H.U. Ruhnau, R. Kirchhof, R. Kiehn, M. Müller, A. Schreyer, The high energy materials science beamline (HEMS) at PETRA III, *AIP Conf. Proc.* 1234 (2010) 391–394. doi:10.1063/1.3463221.
- [29] M. Basham, J. Filik, M.T. Wharmby, P.C.Y. Chang, B. El Kassaby, M. Gerring, J. Aishima, K. Levik, B.C.A. Pulford, I. Sikharulidze, D. Sneddon, M. Webber, S.S. Dhesi, F. Maccherozzi, O. Svensson, S. Brockhauser, G. Náray, A.W. Ashton, Data Analysis Workbench (DAWN), *J. Synchrotron Radiat.* 22 (2015) 853–858. doi:10.1107/S1600577515002283.
- [30] J. Filik, A.W. Ashton, P.C.Y. Chang, P.A. Chater, S.J. Day, M. Drakopoulos, M.W. Gerring, M.L. Hart, O.V. Magdysyuk, S. Michalik, A. Smith, C.C. Tang, N.J. Terrill, M.T. Wharmby, H. Wilhelm, Processing two-dimensional X-ray diffraction and small-angle scattering data in DAWN 2, *J. Appl. Crystallogr.* 50 (2017) 959–966. doi:10.1107/S1600576717004708.
- [31] D. Balzar, H. Ledbetter, Voigt-function modeling in fourier analysis of size- and strain-broadened X-ray diffraction peaks, *J. Appl. Crystallogr.* 26 (1993) 97–103. doi:10.1107/S0021889892008987.
- [32] H. Liu, J. Liu, SP2: a computer program for plotting stereographic projection and exploring crystallographic orientation relationships, *J. Appl. Crystallogr.* 45 (2012) 130–134. doi:10.1107/S0021889811049582.
- [33] M.K. Miller, A. Cerezo, M.G. Hetherington, G.D.W. Smith, *Atom probe field ion microscopy*, Clarendon Press, Oxford, 1996.
- [34] K. Babinsky, R. De Kloe, H. Clemens, S. Primig, A novel approach for site-specific atom probe specimen preparation by focused ion beam and transmission electron backscatter diffraction, *Ultramicroscopy*. 144 (2014) 9–18. doi:10.1016/j.ultramic.2014.04.003.
- [35] T.D. Bigg, D.K. Matlock, J.G. Speer, D.V. Edmonds, Dynamics of the quenching and partitioning (Q&P) process, *Solid State Phenom.* 172–174 (2011) 827–832. doi:10.4028/www.scientific.net/SSP.172-174.827.
- [36] M.C. Somani, D.A. Porter, L.P. Karjalainen, R.D.K. Misra, On various aspects of decomposition of austenite in a high-silicon steel during quenching and partitioning, *Metall. Mater. Trans. A*. 45 (2014) 1247–1257. doi:10.1007/s11661-013-2053-8.
- [37] H.Y. Li, X.W. Lu, X.C. Wu, Y.A. Min, X.J. Jin, Bainitic transformation during the two-step quenching and partitioning process in a medium carbon steel containing silicon, *Mater. Sci. Eng. A*. 527 (2010) 6255–6259. doi:10.1016/j.msea.2010.06.045.
- [38] E. De Moor, J. Penning, Alloy design for enhanced austenite stabilization via quenching and partitioning, in: *Int. Conf. New Dev. Adv. High-Strength Sheet Steels*, Warrendale, USA, 2008: pp. 199–207.
- [39] card number 00-035-0772 of the ICDD-PDF 2 (release 2018), (n.d.).
- [40] card number 01-075-6674 of the ICDD-PDF 2 (release 2018), (n.d.).
- [41] card number 01-089-3689 of the ICDD-PDF 2 (release 2018), (n.d.).
- [42] card number 00-036-1248 of the ICDD-PDF 2 (release 2018), (n.d.).
- [43] card number 00-038-1364 of the ICDD-PDF 2 (release 2018), (n.d.).
- [44] card number 01-076-8401 of the ICDD-PDF 2 (release 2018), (n.d.).
- [45] Y.A. Bagaryatskii, Possible mechanism of martensite decomposition, *Dokl. Akad. Nauk SSSR*. 73 (1950) 1161–1164.
- [46] I.V. Isaichev, Orientation between cementite and ferrite, *Zh Tekhnicheskoi Fiz.* 17 (1947).
- [47] M. Gouné, S. Aoued, F. Danoix, G. Geandier, A. Poulon-Quintin, J.C. Hell, M. Soler, S.Y.P. Allain, Alloying-element interactions with austenite/martensite interface during quenching and partitioning of a model Fe-C-Mn-Si alloy, *Scr. Mater.* 162 (2019) 181–184. doi:10.1016/j.scriptamat.2018.11.012.
- [48] A.J. Clarke, M.K. Miller, R.D. Field, D.R. Coughlin, P.J. Gibbs, K.D. Clarke, D.J. Alexander, K.A. Powers, P.A. Papin, G.

- Krauss, Atomic and nanoscale chemical and structural changes in quenched and tempered 4340 steel, *Acta Mater.* 77 (2014) 17–27. doi:10.1016/j.actamat.2014.05.032.
- [49] D.T. Pierce, D.R. Coughlin, K.D. Clarke, E. De Moor, J. Poplawsky, D.L. Williamson, B. Mazumder, J.G. Speer, A. Hood, A.J. Clarke, Microstructural evolution during quenching and partitioning of 0.2C-1.5Mn-1.3Si steels with Cr or Ni additions, *Acta Mater.* 151 (2018) 454–469. doi:10.1016/j.actamat.2018.03.007.
- [50] J.G. Speer, A.L. Araujo, D.K. Matlock, E. de Moor, Nb-microalloying in next-generation flat-rolled steels: An overview, *Mater. Sci. Forum.* 879 (2016) 1834–1840. doi:10.4028/www.scientific.net/MSF.879.1834.
- [51] N. Zhong, X.D. Wang, L. Wang, Y.H. Rong, Enhancement of the mechanical properties of a Nb-microalloyed advanced high-strength steel treated by quenching-partitioning-tempering process, *Mater. Sci. Eng. A.* 506 (2009) 111–116. doi:10.1016/j.msea.2008.11.014.
- [52] X.D. Wang, W.Z. Xu, Z.H. Guo, L. Wang, Y.H. Rong, Carbide characterization in a Nb-microalloyed advanced ultrahigh strength steel after quenching-partitioning-tempering process, *Mater. Sci. Eng. A.* 527 (2010) 3373–3378. doi:10.1016/j.msea.2010.02.026.
- [53] R.D.K. Misra, H. Zheng, K.M. Wu, L.P. Karjalainen, Niobium-containing quenching and partitioning processed ultrahigh strength martensite-austenite dual phase steels, *Mater. Sci. Eng. A.* 579 (2013) 188–193. doi:10.1016/j.msea.2013.05.043.
- [54] J. Zhang, H. Ding, R.D.K. Misra, C. Wang, Microstructural evolution and consequent strengthening through niobium-microalloying in a low carbon quenched and partitioned steel, *Mater. Sci. Eng. A.* 641 (2015) 242–248. doi:10.1016/j.msea.2015.06.050.
- [55] J. Dong, X. Zhou, Y. Liu, C. Li, C. Liu, H. Li, Effects of quenching-partitioning-tempering treatment on microstructure and mechanical performance of Nb-V-Ti microalloyed ultra-high strength steel, *Mater. Sci. Eng. A.* 690 (2017) 283–293. doi:10.1016/j.msea.2017.03.020.
- [56] S. Suzuki, Features of transmission EBSD and its application, *JOM.* 65 (2013) 1254–1263. doi:10.1007/s11837-013-0700-6.
- [57] P.W. Trimby, Orientation mapping of nanostructured materials using transmission Kikuchi diffraction in the scanning electron microscope, *Ultramicroscopy.* 120 (2012) 16–24. doi:10.1016/j.ultramic.2012.06.004.
- [58] M. Herbig, P. Choi, D. Raabe, Combining structural and chemical information at the nanometer scale by correlative transmission electron microscopy and atom probe tomography, *Ultramicroscopy.* 153 (2015) 32–39. doi:10.1016/j.ultramic.2015.02.003.
- [59] M. Dirand, L. Afqir, Identification structurale precise des carbures precipites dans les aciers faiblement allies aux divers stades du revenu - mecanismes de precipitation, *Acta Metall.* 31 (1983) 1089–1107.
- [60] A. Königer, C. Hammerl, M. Zeitler, B. Rauschenbach, Formation of metastable iron carbide phases after high-fluence carbon ion implantation into iron at low temperatures, *Phys. Rev. B.* 55 (1997) 8143–8147.
- [61] C. Hammerl, A. Königer, B. Rauschenbach, Electronmicroscopical study of the formation of iron carbide phases after high-fluence carbon ion implantation into iron at low temperatures, *J. Mater. Res.* 13 (1998) 2614–2622.
- [62] T. Waterschoot, K. Verbeken, B.C. de Cooman, Tempering kinetics of the martensitic phase in DP steel, *ISIJ Int.* 46 (2006) 138–146.
- [63] C.-B. Ma, T. Ando, D.L. Williamson, G. Krauss, Chi-Carbide in tempered high carbon martensite, *Metall. Trans. A.* 14 (1983) 1033–1045.
- [64] J. Hidalgo, K.O. Findley, M.J. Santofimia, Thermal and mechanical stability of retained austenite surrounded by martensite with different degrees of tempering, *Mater. Sci. Eng. A.* 690 (2017) 337–347. doi:10.1016/j.msea.2017.03.017.